Geophysical Journal International

Geophys. J. Int. (2023) **234,** 1617–1627
Advance Access publication 2023 April 11
GJI Seismology

https://doi.org/10.1093/gji/ggad155

Source mechanisms and induced seismicity in the Val d'Agri Basin (Italy)

P. Roselli,[1] L. Improta,[2] G. Kwiatek,[3] P. Martínez-Garzón,[3] G. Saccorotti[4] and A. M. Lombardi[1]

[1] *Istituto Nazionale di Geofisica e Vulcanologia, Sezione Roma* 1, *Roma* 00143, *Italy. E-mail: pamela.roselli@ingv.it*
[2] *Istituto Nazionale di Geofisica e Vulcanologia, Osservatorio Nazionale Terremoti, Roma* 00143, *Italy.*
[3] *Helmholtz Centre Potsdam, GFZ German Research Centre for Geoscience, Potsdam* 14473, *Germany.*
[4] *Istituto Nazionale di Geofisica e Vulcanologia, Sezione di Pisa, Pisa* 56125, *Italy* .

Accepted 2023 April 4. Received 2023 March 25; in original form 2022 March 30

SUMMARY

We present the results from a fully unconstrained moment tensor inversion of induced seismic events in a complex and high seismic hazard region (Val d'Agri basin, Southern Italy). The study area hosts two well-documented cases of induced microseismicity linked to (i) a wastewater injection well of a giant oilfield (the largest in onshore Europe), and (ii) severe seasonal level changes of an artificial lake. In order to gather information on the non-double-couple components of the source and to better understand the rupture mechanisms, we analyse seismic events recorded during daily injection tests in the disposal well. The computed moment tensors have significant non-double-couple components that correlate with the well-head injection pressure. The injection parameters strongly influence the rupture mechanism that can be interpreted as due to the opening/closing of a fracture network inside a fault zone of a pre-existing thrust fault. For the case of the reservoir-induced seismicity, no direct correlations are observed with the loading/unloading of the reservoir.

Key words: Earthquake source observations; Induced seismicity.

1 INTRODUCTION

Seismic moment tensor inversion is one of the best ways to better understand, investigate and compare the governing seismic source processes and its kinematics. The full seismic moment tensor (FMT) is defined as a symmetric tensor M_{ij} (3×3 matrix) composed by nine generalized force couples (Aki & Richards 2002) and six independent moment tensor components which represent different types of seismogenic processes such as earthquakes, explosions, implosions, rock falls or mixed-mode ruptures driven by fluid and gas injections. Traditionally, earthquake sources are considered as simple pure shear failures, characterized a by double-couple (DC) seismic moment tensor model M_{ij}, with $|M_{ij}| = 0$ and tr(M) = 0. Some physical mechanisms can also produce non-double-couple (NDC) components under specific conditions, for example presence of fluids in the source area, fracture opening and closing, mineralogical phase transitions within the seismogenic crust, rupture of non-planar fault surfaces. In recent years, it became gradually accepted that significant NDC components may contribute to deformation in the earthquake source region (Frohlich 1994). Then, the FMT may be decomposed using different schemes, for example a decomposition into isotropic (ISO), compensated linear vector dipole (CLVD) and DC components (Knopoff & Randall 1970). Changes in the seismic source volume during faulting leads to the existence of ISO components (e.g. Frohlich 1994; Julian *et al.* 1998; Miller *et al.* 1998), expressed as non-zero trace of the eigenvalues of the seismic moment tensor. The DC represents the pure shear motion from two orthogonal vector pairs of equal magnitude but opposite sign; the ISO represents the isotropic volumetric change in the crack closures or implosions; the CLVD represents motion away (if positive) or toward (if negative) the earthquake sources with no net volume change and generally complex physical interpretation (Frohlich 1994; Julian *et al.* 1998; Martínez-Garzón *et al.* 2017). The NDC percentage in the source constitutes the sum of absolute ISO and CLVD components so that %NDC = |%ISO| + |%CLVD| and |%ISO|+|%CLVD|+%DC = 100%. It is currently known that mixed, shear-tensile earthquakes nucleate in geothermal and volcanic zones rich in fluids under overpressure conditions (Ross *et al.* 1996; Saraò *et al.* 2010), during hydraulic fracturing, fluid injection experiments (Zoback 2007; Fischer & Guest 2011; Ellsworth 2013; Martínez-Garzón *et al.* 2017; Dost *et al.* 2020; Kühn *et al.* 2020) and wastewater disposal activities (Amemoutou *et al.* 2021). Significant contribution of NDC components has been found by examination of sources of induced earthquakes; for instance, NDC components greater than 25% in the 65% of the total analysed moment tensors are obtained in Martínez-Garzón *et al.* (2017). In particular, for

© The Author(s) 2023. Published by Oxford University Press on behalf of The Royal Astronomical Society.

Downloaded from https://academic.oup.com/gji/article/234/3/1617/7115318 by INGV user on 25 May 2023

injection-induced events, the information on the volumetric component of the seismic sources is critical to understand the role of fluids and pore pressure changes on the rupture process.

In this study, we investigate both DC and NDC components of induced micro-earthquakes in the tectonically complex Val d'Agri area (Southern Italy; see Fig. 1).

2 REGION BACKGROUND AND DATA

The Val d'Agri is a Quaternary extensional basin located in the Southern Apennines fold-and-thrust belt. It is a relevant area of study because of: (i) its complex tectonic evolution (i.e. Royden *et al.* 1987), (ii) the presence of the largest oilfield in onshore Europe, (iii) the occurrence of spatial swarms of low-magnitude seismic events induced by fluid injection in the oilfield and of small events associated with variations in level of a nearby reservoir (Valoroso *et al.* 2009; Stabile *et al.* 2014a, b; Improta *et al.* 2015; Improta *et al.* 2017; Hager *et al.* 2021) and (iv) the high seismic hazard, as documented by the occurrence of M6+historical earthquakes (Rovida *et al.* 2020, 2021).

Although recent seismicity has been investigated by several studies (Improta *et al.* 2017, and references therein), so far information on source mechanisms of natural and induced local events have been derived from standard inversion of first *P*-wave polarities (Valoroso *et al.* 2009; Improta *et al.* 2017), which by default produce DC-constrained solutions. The study area hosts two well-documented cases of induced seismicity: (i) fluid injection induced microseismicity (IIS) linked to the Costa Molina 2 wastewater disposal well (CM2) that spatially relates to a pre-existing thrust fault (Buttinelli *et al.* 2016), and (ii) protracted reservoir induced seismicity (RIS), correlated with significant seasonal oscillation of the water level in the Pertusillo artificial lake (Stabile *et al.* 2014a, Figs 1a and b). Our systematic analysis of the earthquake source mechanisms employing FMT inversion aims to better understand the rupture process of induced events originating from those two different types of anthropogenic activities. We investigate the role played by fluid pore pressure, local stress changes due to gravitational loading, local geological conditions and stress field on complexity of observed source mechanisms.

2.1 Geological setting

The geological setting of the Val d'Agri is characterized by a stack of thrust sheets of 2–4 km thickness consisting of Meso-Cenozoic pelagic and carbonatic platform sequences. These deeply deformed units tectonically cover the Inner Apulia Platform (IAP) that consists of Mesozoic–Miocene shallow water carbonates deformed by a NE-verging system of thrusts and folds dating back to Late Pliocene–Early Pleistocene (Fig. 1b). After this compressive tectonic phase, the region has undergone an extensional regime documented by the development of normal fault systems that bound the Val d'Agri continental basin (Improta *et al.* 2010, and references therein). The study area is characterized by an NE-trending extensional stress field (SH_{max} $\sim$ NW-SE) consistent with the regional SW-NE extension of the Apennines range; this local stress regime is inferred by field structural analysis, borehole breakouts, seismic anisotropy parameters (Pastori *et al.* 2009) and GPS data (Cucci *et al.* 2004; Maschio *et al.* 2005; Montone *et al.* 2012; Ferranti *et al.* 2014). The region was struck by a destructive M7 earthquake in 1857 (Rovida *et al.* 2020) and the natural seismicity recorded in the last 40 yr consists of sparse events occurring in the upper crust that seldom exceed M3 (ISIDE working Group 2007).

2.2 Data

The seismic waveforms analysed in this study were recorded by a temporary local network complementing the permanent national network operated by the Istituto Nazionale di Geofisica e Vulcanologia (INGV) between 2005 May and 2006 June (Valoroso *et al.* 2009, Fig. 1c). The temporary network consists of 23 three-component short-period stations equipped with Lennartz-5 sec velocimeters (sampling rate 125 Hz) with apertures around 5–8 km. The 2005–2006 survey provided a high-quality catalogue (magnitude of completeness $M_c \sim 0.4$) including spatial clusters of low magnitude events ($M_L \leq 2.7$) accurately located using a high-resolution 3-D velocity model derived from a local earthquake tomography (Improta *et al.* 2017). These events occur close to the wastewater injection well CM2 of the oilfield and to the southwest of the Pertusillo artificial lake. We divided our data set into two different spatial clusters according to the respective causative process: the CM2 cluster (i.e. IIS) and the Pertusillo seismicity (i.e. RIS).

2.2.1 CM2 wastewater disposal seismicity

The Val d'Agri hosts the largest onshore oilfield of Europe. Hydrocarbons are extracted from a fractured and low-porosity reservoir hosted by carbonates of the Apulia Platform at 2–4 km depth. Since 2006 June 1, co-produced saltwater has been disposed through the injection well CM2 drilled into a marginal, unproductive zone of the hydrocarbon reservoir and fluids are re-injected between 3.0 and 3.1 km depth b.s.l. into the Apulia limestones (Improta *et al.* 2017, Fig. 1b). Disposal operations have been carried out with variable injection rates and wellhead pressures reaching maximum values of 2.800–3.000 m^3/day and 130–140 bar, respectively (Improta *et al.* 2015; Hager *et al.* 2021). Given the monthly injected volumes ranging from 60 000 to 80 000 m^3, CM2 can be classified as a long-term, high-rate injection well. Since the first injection tests and up to the removal of the INGV dense temporary network (2006 June 1–12), IIS occurred nearby the well. A causal relationship between fluid injection and seismicity is evidenced by qualitative correlation analysis performed by Improta *et al.* (2017) that compared hourly injection data to the seismicity rate (events occurrence, number and energy). The correlation between seismicity and injection operations has been recently validated through a local coupled flow-geomechanical 3-D modelling and a rate-state model (Hager *et al.* 2021).

The original IIS catalogue consists of a cluster of 69 micro-earthquakes ($0.3 < M_L < 1.8$) located between 3.8–5.1 km depth under the injection well (Improta *et al.* 2017). We selected the events for which both timing and polarity of first arrivals could be unambiguously determined from visual inspection of the vertical component seismograms, Butterworth bandpass filtered (2–50 Hz) frequency band (see Fig. S1, Supporting Information). After this preliminary selection, the data set amounted to 34 events recorded by 14 stations with inter-station distance between 5 and 15 km.

2.2.2 Pertusillo lake seismicity

The Pertusillo artificial lake covers an area of about 75 km^2 and can store up to 150 million m^3 of water (Valoroso *et al.* 2009). Following the initial impoundment in 1963, this medium-size water

Downloaded from https://academic.oup.com/gji/article/234/3/1617/7115318 by INGV user on 25 May 2023

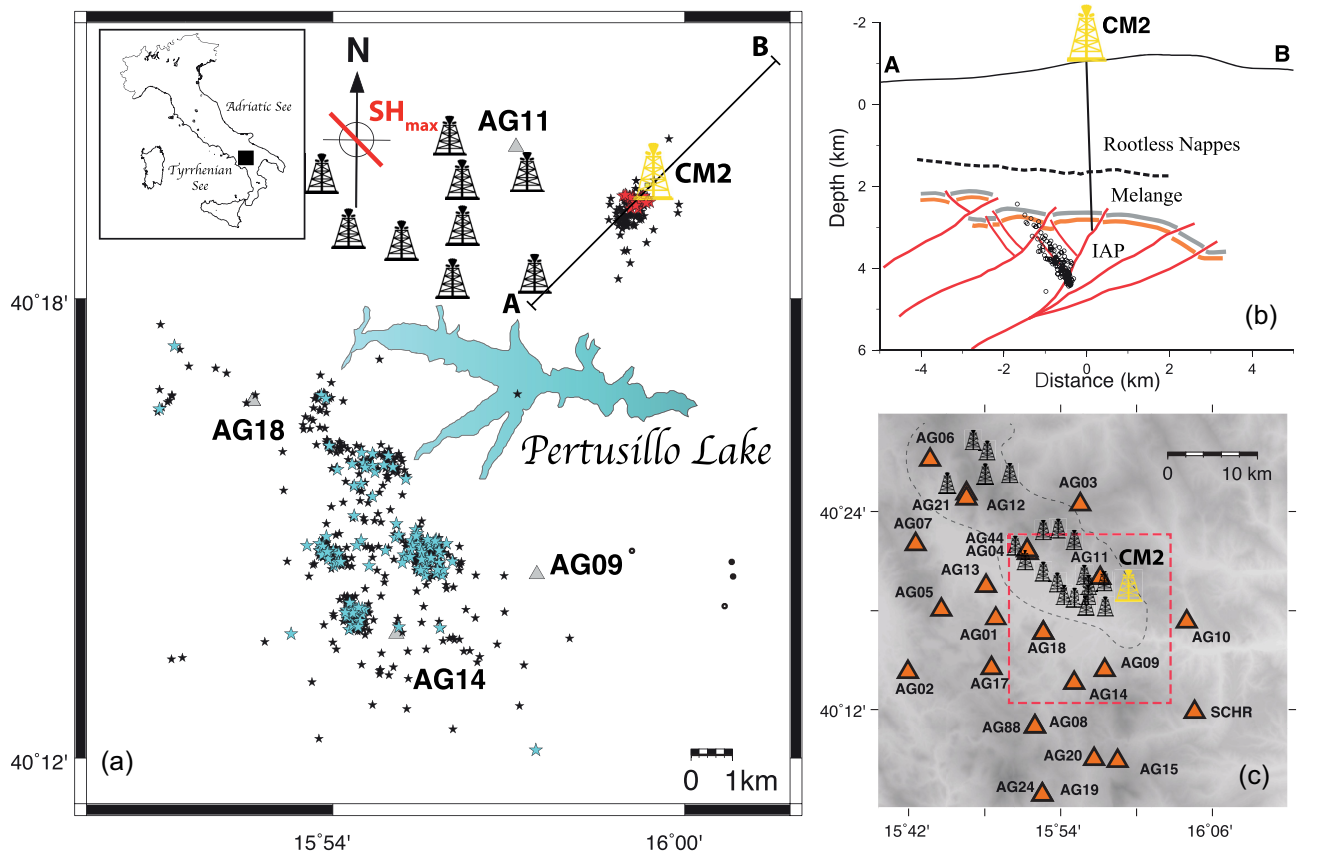

Figure 1. (a) Location map of the study area with seismic stations of the 2005–2006 INGV survey (grey triangles), micro-earthquakes recorded between 2005–2006 and analysed in this study (black stars), the oil production wells (black symbols) and the CM2 injection well (yellow symbol). The events associated with reliable FMT solutions are outlined (Pertusillo RIS, cyan stars; CM2 injection-induced events, red stars). In red, the direction of the maximum horizontal stress (SH_{max}) derived from breakouts from local deep wells that is in agreement with the regional NE trending extensional stress field (Cucci *et al.* 2004; Montone *et al.* 2012); (b) Cross-section tied to the well CM2 (yellow symbol) showing high-precision double-difference locations of injection-induced events recorded by temporary and permanent monitoring networks between 2006 and 2014, with superimposed a structural model of the IAP reservoir (modified from Improta *et al.* 2017, red lines: Pliocene thrust faults and back thrusts; orange line: top reservoir; grey line: top Apulia Pliocene terrigenous deposits; Melange: reservoir seal formed by a tectonic melange (Pliocene overpressured shales); Rootless Nappes: east-verging rootless nappes formed by basinal Meso-Cenozoic deposits overthrusting the tectonic melange; (c) zoom-out of the study area (red dashed square) in panel (a) with all stations of the 2005–2006 passive seismic survey depicted by orange triangles, oil production wells (black symbols); CM2 injection well (yellow symbol) and approximately extension of the oilfield (grey dashed line).

reservoir has experienced seasonal changes of the water level as large as 40 m, corresponding to volume changes on the order of 120 million m^3. Seismic swarms have been recorded since 2001 to the SW of the lake by permanent and temporary INGV stations and by a private local network dedicated to the monitoring of the nearby Val d'Agri oilfield (Valoroso *et al.* 2009; Stabile *et al.* 2014a).

The reservoir impoundment dates back to 1962 and previous analysis of data recorded by sparse regional stations (Cucci *et al.* 2004) suggests that weak seismic activity may have occurred in the study area before the installation of the local network in 2001. The earthquake rates follow the seasonal cycles of refill and emptying of the reservoir (winter–spring and summer–fall, respectively) and seismicity has been interpreted as protracted RIS linked to pore fluid pressure diffusion (Valoroso *et al.* 2011; Stabile *et al.* 2014a). Recently, Rinaldi *et al.* (2020) have shown that the poroelastic response to seasonal volume changes of the Pertusillo reservoir can cause Coulomb stress perturbations above the threshold for inducing seismicity. The original catalogue consists of 526 earthquakes ($-0.2 \leq M_L \leq 2.7$) distributed according to four main spatial clusters located SW of the lake at 2.0–5.5 km depth within the Apulian carbonates (Fig. 1a). We select the best recorded 110 events (with $0.6 \leq M_L \leq 2.7$ and inter-station distance between 5 and 15 km for 23 stations). The analysis was performed on the Butterworth bandpass filtered (2–50 Hz) vertical components.

3 FMT INVERSION AND DATA PROCESSING

Many different methods have been developed to calculate the seismic moment tensor (e.g. Dreger & Helmberger 1993; Andersen 2001, and references therein), but the choice of the most appropriate technique depends strictly on the data characteristics. For small magnitude events ($M < 2$), FMT inversion approaches based on *P*-wave amplitudes are preferable to those based on waveform modelling which are usually hampered by the difficulty in computing reliable high-frequency synthetic waveforms (i.e. Green's function assessment suffers from uncertainties in the velocity/attenuation model) and by the poor signal-to-noise ratio of micro-earthquakes (e.g. Guilhem *et al.* 2014; Bentz *et al.* 2018). Since we are dealing with weak motion recordings ($M_L < 2.7$) of clustered seismicity

Downloaded from https://academic.oup.com/gji/article/234/3/1617/7115318 by INGV user on 25 May 2023

and being interested in both DC and NDC components, we applied the hybridMT technique (Andersen 2001; Kwiatek *et al.* 2016) that uses the first *P*-wave pulse amplitudes to solve for the FMT and has already been used for the analysis of injection-induced clustered microseismicity (e.g. Martínez-Garzón *et al.* 2017; Bentz *et al.* 2018; Amemoutou *et al.* 2021). To account for the poorly known path and site effects between the centroid of clustered events and the stations, the hybridMT algorithm (Kwiatek *et al.* 2016) can be applied to clustered seismicity where the hypocentre separations are small compared to the source-to-receiver distances. Then, we adopted an iterative approach that progressively corrects the observed amplitudes in the presence of any systematic bias related to both experimental and modelling errors. We exclude from the calculation all the stations that did not respect the criteria to obtain reliable results and convergence during the inversion (i.e. good S/N ratio). We limited the analysis to seismic events with a minimum of eight available stations. To calculate ray-lengths, take-off and incidence angles, we used the ray-tracing routines from HypoDD package (Waldhauser 2001) and a selected 1-D velocity model of the Val D'Agri region (Buttinelli *et al.* 2016; Improta *et al.* 2017, Figs S2 and S3, Supporting Information). The resulting seismic moment tensors are decomposed into DC, ISO and CLVD components, expressed in percentage following the decomposition scheme of Knopoff & Randall (1970).

The two data sets and the selected seismic stations are sufficiently suitable for applying the hybridMT inversion, although the CM2 cluster suffers from a poor azimuthal coverage on the northeastern sector. We find that most stations show a polarity match that exceeds 80%. Uncertainties of estimated FMTs are expressed through normalized root-mean-square (RMS) residuals between theoretical and estimated amplitudes (Vavryčuk 2014); for both data sets, the average RMS values are around 0.1–0.2 (Figs S2 and S3, Supporting Information). We executed a further analysis of uncertainties for each parameter discussed (i.e. M_w, %ISO, %CLVD, %DC) by resampling the input data 100 times under assumption that the uncertainty in take-off angles is equal to 5° (cf. Kwiatek *et al.* 2016).

4 RESULTS

The CM2 and Pertusillo data sets (i.e. IIS and RIS) are analysed separately. First, the source mechanisms are classified according to faulting style (Frolich 2001), and then represented in Kaverina Diagrams (Kaverina *et al.* 1996; Álvarez-Gómez 2019) and *P*–*T* polar plots. The CM2 and Pertusillo data sets display different kinematics and distribution of *P*- and *T*-axes (Figs 2a and b, c and d, respectively). In the Kaverina Diagrams, CM2 cluster is located in the Normal/Reverse transition area and it is associated with a nearly horizontal *T*-axis (Fig. 2a), whereas the Pertusillo is mainly characterized by prevailing normal solutions (Fig. 2c).

Most solutions of CM2 earthquakes have ENE-oriented *T*-axes (Figs S4–S6, Supporting Information). The Pertusillo seismicity also includes some reverse faulting mechanisms with variable *T*-axis plunge. The *P*–*T* polar plots illustrate the different distribution of *P* (blue dots) and *T* (red dots) stress axes for the CM2 (Fig. 2b) and Pertusillo (Fig. 2d) seismicity with clustering and quite scattered *P*–*T* axes distributions, respectively. The conventional focal mechanisms representation contains information only about the source orientation; when considering NDC mechanisms it is useful to display the source type without regard to orientation but considering the deviatoric part and the volume change (Julian *et al.* 1998). Then, we use the Hudson plots (see Hudson *et al.* 1989) to display the FMT sources decomposed into the ISO (volume changes) and CLVD (deviatoric) parts without orientation.

The source type plot of CM2 events (Fig. 3a) shows all solutions aligned parallel to the rhomboid side as predicted by the relation of Vavryčuk (2001) that implies moment tensors with equal sign of ISO and CLVD components. We also note that the alignment of Pertusillo sources differs from that of CM2 (Fig. 3b), implying that the two source regions have a different ratio of the Lame's faults constants $\frac{\lambda}{\mu}$ following shear-tensile model proposed by Vavryčuk (2001). From the summary of FMT decompositions obtained for CM2 and Pertusillo source data sets (see Table 1), we observe a strong contribution of both ISO and CLVD components reaching high absolute percentages.

The kinematics of the mechanisms are mostly normal faulting with some reverse mechanism, with a set-up that reflects the plunge in transition normal/reverse (see Fig. 1a). Unlike CM2 earthquakes, the Pertusillo data set also exhibits a few strike-slip faulting mechanisms, (green symbols and beach balls in Fig. 3b).

In a further analysis, we compare the source parameters of the CM2 cluster to injection data (hourly well-head pressure; see Fig. 4). The daily injection tests were performed with a nearly constant hourly rate of 38 m^3/h and progressively longer durations, from 4 h (June 1st) to 33 h (June 7–8st). The peak of wellhead pressure was measured at the end of each test and it reached values increasing from 52 bar (June 1) to 102 bar (June 8).

The comparison reveals the following features: (i) the events with ISO $>$ 0 occur during stages of increasing pressure with the exception of source 7, (ii) the events with large positive volumetric deformation are observed close to the pressure peaks (sources 16, 28, 57 and 59), (iii) the two events with the largest percentage of ISO $>$ 0 occur during the final stage of the main injection test characterized by the maximum pressure of 102 bar (sources 57 and 59, Fig. 4a). Events with negative volumetric deformation are mostly observed at the end of each daily injection test with the exception of the day 8, when both ISO+ and ISO− shear-tensile sources occur during the test (Fig. 4a). This complex behaviour may depend on the complex injection operations carried out between days 7 and 8. Unlike previous daily tests, the injection was not halted in between days 7 and 8. However, the injection rate was strongly reduced during five hours and this produced a stage of decreasing well-head pressure evidenced by a trough of 15 bar (Fig. 4a). This alternation of positive and negative pore fluid pressure changes could explain the complex source mechanisms observed during day 8, when two ISO+ events were followed by earthquakes with negative volumetric deformation, and finally by the two events with the largest ISO+ component and energy (M_w = 2.0–2.2) close to the pressure peak at the end of the injection test.

Positive CLVD percentages are observed during all stages of injection pressure (Fig. 4b). In conclusion, we observe a general correlation between the type of shear-tensile sources and injection operations: positive volumetric deformations occur during stages of increasing pressure and/or close to the daily pressure peak, while stages of decreasing pressure following each daily test are characterized by negative volumetric deformations. This finding points towards a mechanism of fracture opening and closure governed by positive/negative pore fluid pressure changes in the region where events occur.

We also find a relation between the source mechanisms and the event moment magnitude (Fig. 4c): the three shear-tensile sources (sources 28, 57 and 59) show the largest magnitude ($1.9 < M_w < 2.2$). The evident shear-tensile solutions of the largest events (sources 28 and 57) point to the opening of fractures in

Downloaded from https://academic.oup.com/gji/article/234/3/1617/7115318 by INGV user on 25 May 2023

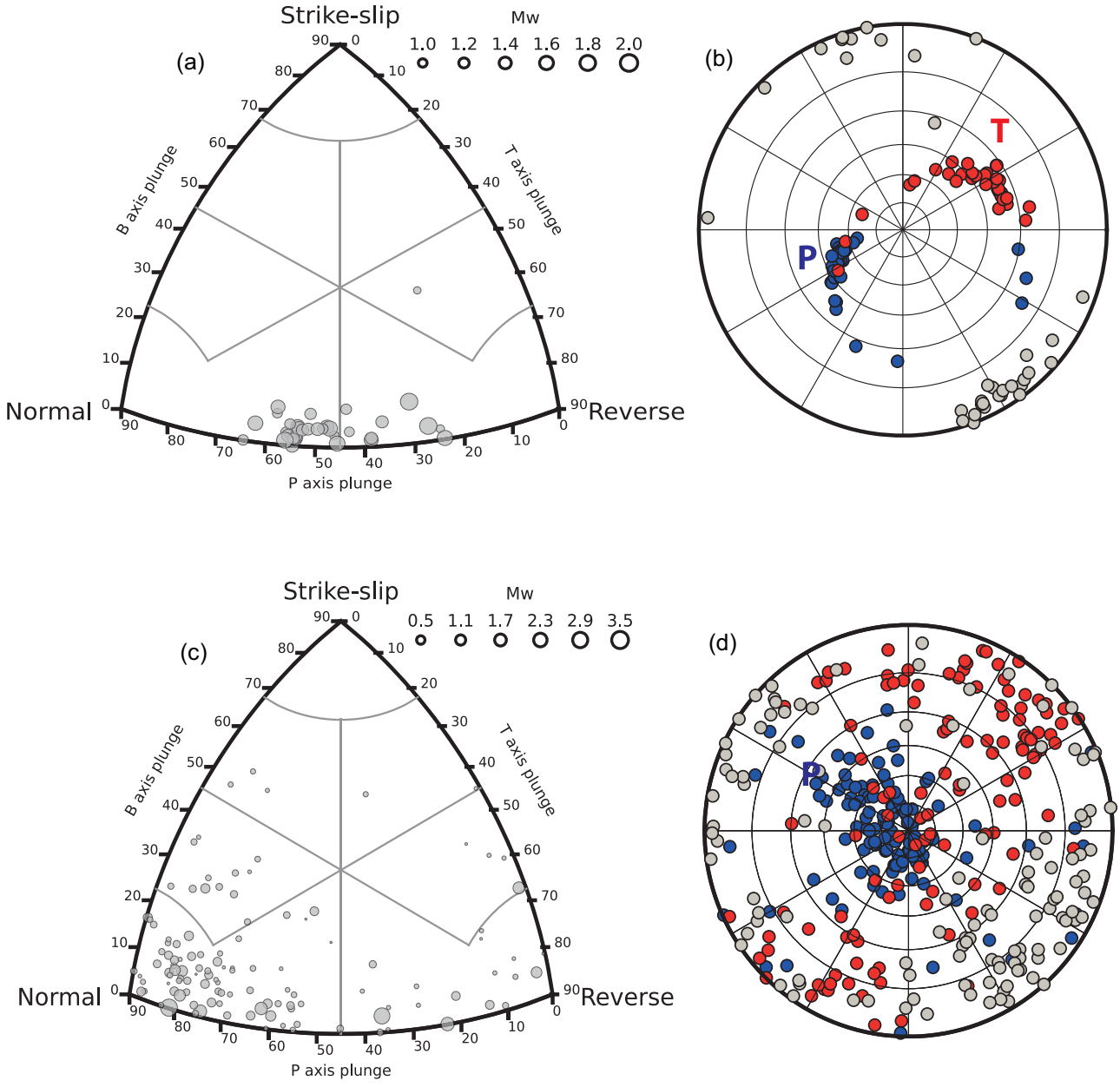

Figure 2. Classifications of the seismic sources selected for the inversion. (a) and (c) Kaverina Diagrams showing faulting style of CM2 (a) and Pertusillo (c) earthquakes. The circle's size is scaled according to the M_w of events; (b) and (d) *P*–*T* polar plots of the CM2 (c) and Pertusillo (d) data sets. Axes are defined by colours: *P* (blue), *T* (red) and *B* (grey), respectively.

concomitance with injection peaks (days 6 and 8). Conversely, earthquakes occurring after the injection tests (i.e. during stages of decreasing pressure) exhibit a normal faulting mechanism, with negative ISO and CLVD components that suggest fracture closing. Probably, the type of faulting mechanism may not be significant because those events lay in a transition region (from normal to reverse kinematics) of the Kaverina diagram (Fig. 2a).

The source parameters of the Pertusillo seismicity are compared to the seasonal water level changes in the lake in Fig. 5. The temporal distribution of NDC components is scattered and no correlation between ISO and CLVD and the water level is visible in Figs 5(a) and (b).

The strong contribution of ISO and CLVD components does not seem to be related to the lake level, and in some cases ISO and CLVD show different polarities. In Fig. 5(c), we analyse the evolution of the ISO component with the M_w obtained after FMT inversion. The plot illustrates that the largest ISO (either positive or negative) components are associated with the highest M_w values. The computed focal mechanisms are mainly normal, in agreement with the active NE-SW trending extensional stress regime (see Fig. 1).

5 ROBUSTNESS OF NON-DOUBLE-COUPLE COMPONENTS

In this section, we attempt to quantify the resolution of the retrieved NDC components for both CM2 and Pertusillo data sets. We estimate the significance of misfit reduction from DC (constrained solution) to FMT inversions by the Bayesian information criterion

Downloaded from https://academic.oup.com/gji/article/234/3/1617/7115318 by INGV user on 25 May 2023

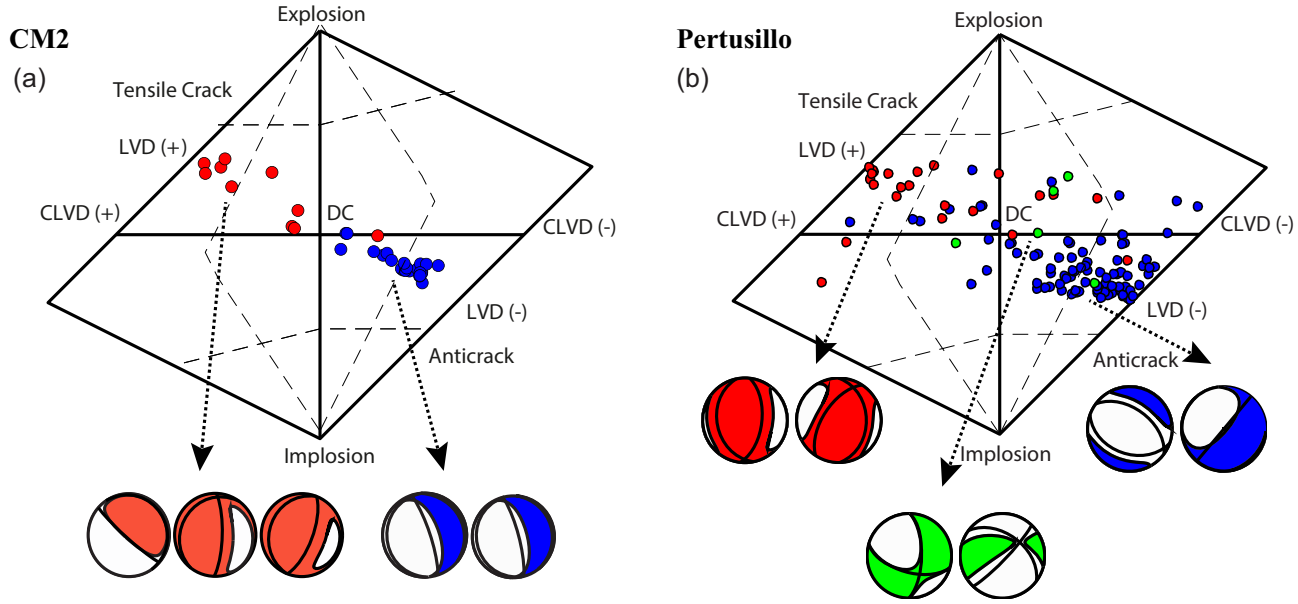

Figure 3. Hudson plots showing results of FMT decomposition for the (a) CM2 and (b) Pertusillo data sets. Dashed lines indicate the representative focal mechanisms corresponding to the Hudson classifications. The colour of the circles and focal mechanisms defines the classical faulting mechanism: normal (blue), reverse (red) and strike-slip (green), respectively.

Table 1. FMT decompositions for CM2 and Pertusillo data sets.

	ISO+ (%)	ISO− (%)	CLVD+ (%)	CLVD− (%)	|ISO| > 20(%)	|CLVD| > 20(%)
CM2	24	74	24	74	53	83
PERTUSILLO	29	71	25	75	47	84

(BIC; Kass & Raftery 1995), defined as:

$$\mathrm{BIC} = k\ln(n) + n\ln\left(\frac{R}{n}\right) \quad (1)$$

in which k is the number of free moment tensor components plus 1 ($4+1$ for DC-constrained and $6+1$ for the FMT), n is the number of polarities and R is the mean-square error of the inversion (see also Cesca *et al.* 2012; Bentz *et al.* 2018). The preferred solution is the model with lowest BIC value**,** whereas the penalized solution is the model with a larger number of free parameters. In Fig. 6, we show the BIC values calculated for both CM2 and Pertusillo data sets. All the analysed CM2 sources fall within the FMT domain, except for four cases which are located close to the boundary line (Fig. 6a). Remarkably, sources no. 57, 59 and 28, showing the highest values of %NDC components, fall in the FMT domain (see Figs 3a and b). The distinction between two models is less clear for the Pertusillo case. About 33% of sources (36 out of 110) have preferred DC mechanisms, although the BIC of the two models are very close (Fig. 6b). Thus, we may conclude that the BIC suggests a strong statistical significance of the results from the CM2 seismicity. Such significance is less robust in the Pertusillo case, in accordance with the lack of clear correlation between the impoundment parameters and the retrieved source mechanisms.

A more formal, statistical way to compare nested models is given by the likelihood-ratio test (LRT), which, beside to deciding whether the FMT solution is favoured over the simpler DC model, offers the chance for formal rejection thresholds (see Supporting Information).

The LRT statistic, given by

$$\mathrm{LR} = -2 * \mathrm{n} * [\ln(\mathrm{R_{DC}}/\mathrm{n}) - \ln(\mathrm{R_{FMT}}/\mathrm{n})] \quad (2)$$

where $\mathrm{R_{DC}}$ and $\mathrm{R_{FMT}}$ are the mean-square error of DC and FMT inversion, respectively. LRT approximately follows a χ^2 distribution with 2 degrees of freedom corresponding to the difference in the number of free parameters between the more complex, FMT model and the simpler DC mechanism. Using this information, we can determine the critical values of the LRT and, then, quantify the significance of misfit reduction given by the FMT inversion.

Application of LRT statistics to the CM2 and Pertusillo data sets provides different results. For the CM2 data set, the LR statistic is larger than the 95$^{\mathrm{th}}$ (99$^{\mathrm{th}}$) percentile of the χ^2 distribution for most events, suggesting that the FMT model is required to thoroughly explain the observations. A small subset of events (namely, events 11, 13, 26 and 60) lies below the 99$^{\mathrm{th}}$ percentile boundary and therefore they can be satisfactory interpreted using the simpler DC mechanism (Fig. 6c). The resolution of NDC components is more questionable for Pertusillo events (Fig. 6d). In that case, a significant portion of the recorded events exhibits LR values are too low to buttress the FMT model.

6 DISCUSSIONS

FMT of the seismicity induced by fluid injection into the CM2 disposal well and by level changes in the Pertusillo water reservoir are characterized by a significant percentage of NDC components for most of the events. For CM2 injection induced seismicity, about 80% of the sources have NDC $\geq$ 30%, with negative and positive ISO components reaching values of -27 and 33%, respectively. For Pertusillo data (RIS), about 90% of the sources have NDC $\geq$ 30% and the determined ISO reaches extreme values of -33 and 35%.

6.1 The role of pore fluid pressure on the CM2 earthquake source mechanisms

Results obtained for the cluster of micro-earthquakes recorded during the first injection tests in the CM2 disposal well provide valuable

Downloaded from https://academic.oup.com/gji/article/234/3/1617/7115318 by INGV user on 25 May 2023

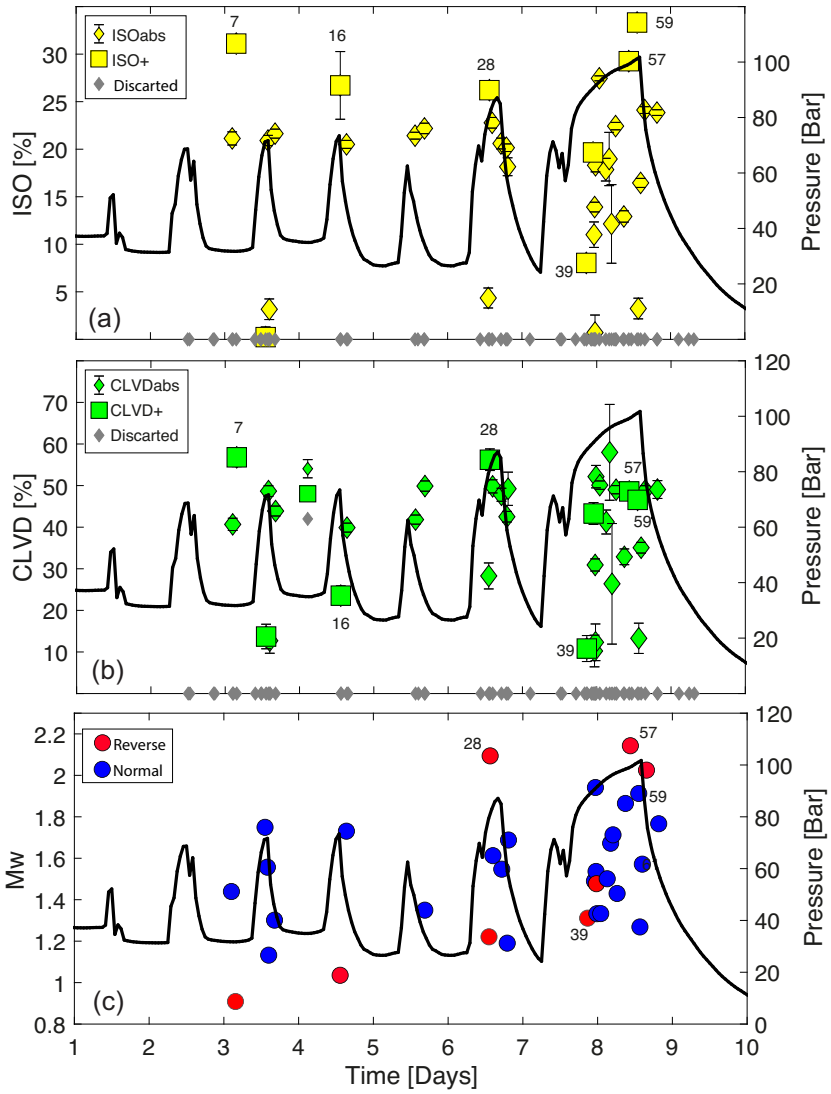

Figure 4. Comparison of the NDC components and M_w with hourly injection data (well head pressure) of the CM2 well. The black curve represents the hourly pressure data as a function of ISO, CLVD and M_w values computed for each selected event. (a) The positive (yellow squares) and absolute ISO (yellow diamond) components with error bars. (b) The positive (green squares) and absolute CLVD (green diamond) components with error bars. (c) The M_w (dots not scaled with M_w) with the related full normal (blue dots) and reverse (red dots) focal mechanisms. The numbers indicate the index of events of particular interest. The grey diamonds in the bottom display the events discarded after signal-to-noise selection.

information for a better understanding of the sources of these fluid-injection induced events. According to Improta *et al.* (2017), the induced seismicity related to the CM2 well originated from the rupturing of small faults and fractures in a highly permeable fault zone that underwent a pressure channelling effect. Our results show a high percentage of both ISO and CLVD components with also marked negative values associated with small magnitudes. We interpret the negative ISO components as an index of decreasing volume, which should be expected in a compacting medium. Similar results in comparable conditions were also obtained in a hydrocarbon-induced seismicity experiment in the Groningen Gas Field (Dost *et al.* 2020; Kühn *et al.* 2020) and wastewater disposal activities in Southern Kansas, US (Amemoutou *et al.* 2021). The non-zero ISO and CLVD components are attributable to a shear-tensile model of the sources (Vavryčuk 2001). From a structural point of view, the 3-D subsurface model of the crustal volume around CM2 well (Buttinelli *et al.* 2016), together with the seismological analysis of Improta *et al.* (2017), indicate that: (i) the carbonate reservoir is deformed by at least four NW-trending, SW-dipping moderate- to high-angle reverse faults with associated NE-dipping back-thrusts. All these faults are inherited structures dating back to the Late Pliocene–Early Pleistocene compressional tectonics; (ii) the CM2 seismic sources are concentrated within the carbonate reservoir where brines are re-injected, they align in the SSW-NNE direction and define a NE-dipping fault zone 200–300 m thick (Improta *et al.* 2017) and (iii) the induced earthquakes mostly align on one of the back-thrusts, and have prevailing extensional focal mechanisms with highly variable strike and dip values. Such a fault zone encompasses the pre-existing back-thrust that is favourably oriented in the present extensional stress field (Buttinelli *et al.* 2016).

As indicated by a pronounced low-*Vp*, high-*Vp*/*Vs* anomaly unravelled by a reservoir-scale passive seismic tomography (Improta *et al.* 2017), the fault zone is confined within the brine-saturated carbonate reservoir characterized by a widespread network of open and conductive fractures that allowed the rapid propagation of the pore fluid pressure perturbations from the wellbore to the source

Downloaded from https://academic.oup.com/gji/article/234/3/1617/7115318 by INGV user on 25 May 2023

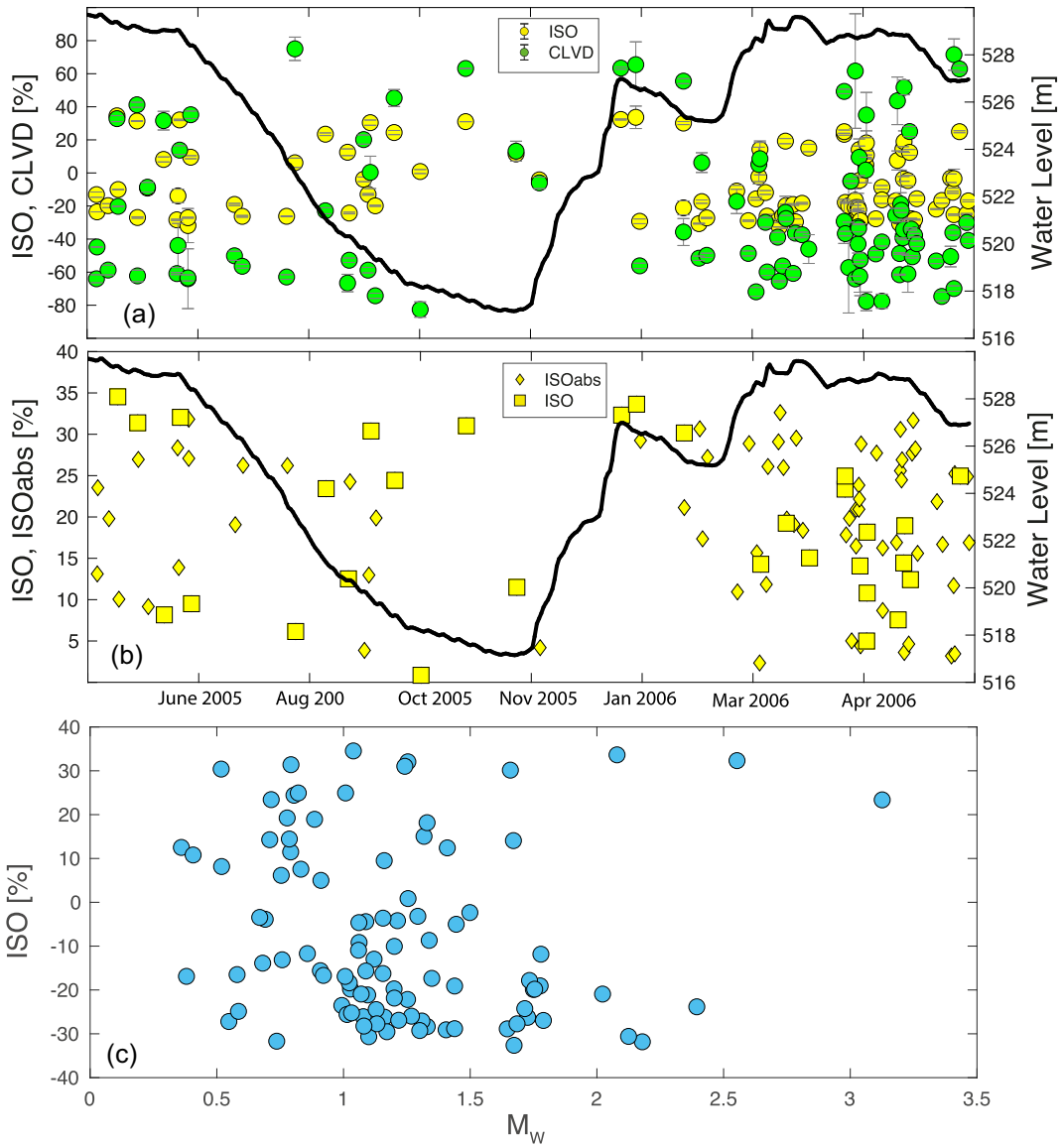

Figure 5. The seismic moment tensor decompositions of the seismicity in the Pertusillo region. Comparison of ISO (yellow dots), CLVD (green dots) percentage (a), ISO positive and absolute percentage (b) with the daily water level (black line) of the Pertusillo lake for 1 yr (2005–2006). (c) The comparison of the ISO component with the M_w (light blue dots) computed from FMT inversion.

region (i.e. the fault zone). A pressure channelling effect has been recently invoked by Hager *et al.* (2021) to model the CM2 well injection induced seismicity. A detailed geomechanical modelling targeting the injection zone indicates that the favourably oriented back-thrust underwent a rapid pressurisation causing a change in Coulomb failure stress of the order of 0.5 MPa during the first stage of injection. Taken together, the results from Buttinelli *et al.* (2016), Improta *et al.* (2017) and Hager *et al.* (2021) provide compelling evidence of a pre-existing thrust fault reactivated in the current extensional regime due to pore fluid pressure perturbations caused by injection operations. However, rather than reactivating a main planar fault, earthquake locations, magnitudes and source mechanisms point to the rupture of small faults and fractures having variable geometries, which belong to a complex fault zone associated to the inherited thrust.

The evident shear-tensile sources obtained in our study by FMT inversion and the general correlation found between hourly injection data and source characteristics (NDC components, faulting mechanisms and moment magnitude, Fig. 4) point to a key role played by fluids and pore-pressure changes in the rupture mechanisms of the CM2 induced seismicity. This result allows improving understanding of the following main observations of Improta *et al.* (2017) and Hager *et al.* (2021): (i) the quasi-instantaneous onset of seismicity, (ii) the strict correlation existing between earthquake rate and injection data, (iii) the rapid response of the seismicity to changes in injection operations and (iv) the rupture of small faults and fractures of an inherited fault zone characterized by variable strike and dip. In this case, the pore pressure perturbations propagating within the highly permeable fracture network of the fault zone could have been strong enough (see also Vadacca 2020; Hager *et al.* 2021) to activate also small structures not optimally oriented in the local stress field. The shear-tensile sources can attain both positive and negative volumetric deformation that relate to stages of increasing and decreasing pore fluid pressure into the fault zone, respectively,

Downloaded from https://academic.oup.com/gji/article/234/3/1617/7115318 by INGV user on 25 May 2023

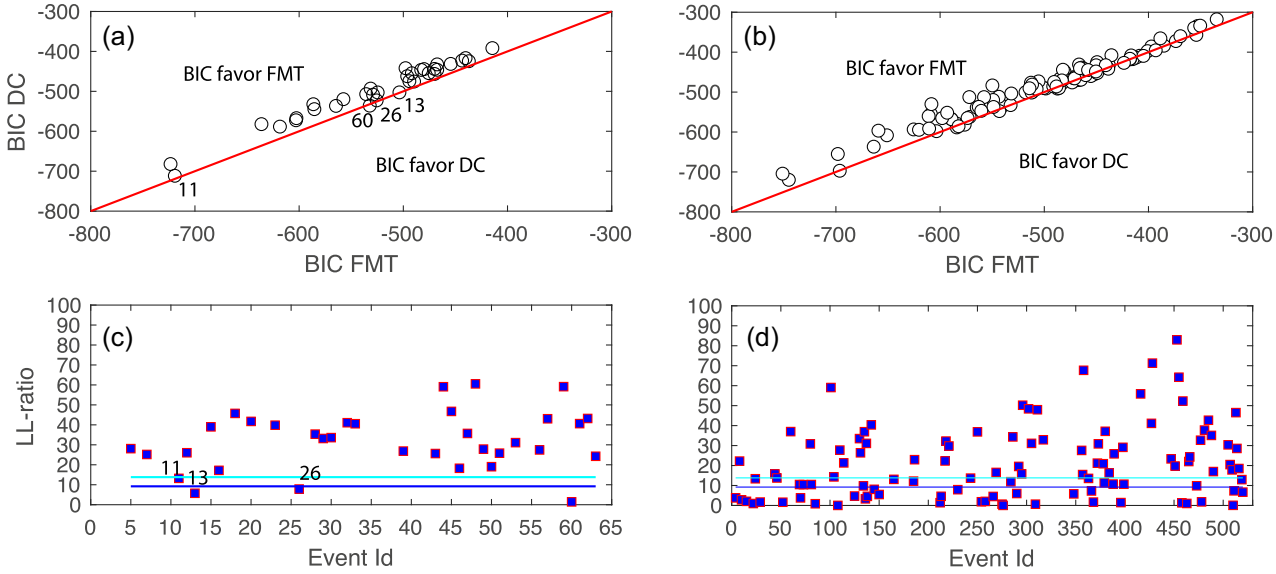

Figure 6. Results of BIC and LRT for the CM2 and Pertusillo data set. (a) BIC values computed for CM2 data set. The *x*- and *y*-axes show the BIC values obtained for FMT and DC constrained inversion, respectively. The red dashed lines separate sources for which BIC favours the pure DC solutions, rather than the FMT ones. (b) The same as in (a), but for Pertusillo events. (c) Values of LR versus event IDs for the CMT database (blue squares). The blue and cyan solid lines mark the 95th and 99th percentile, respectively, of the expected χ^2 distribution. (d) The same of (c), but for the Pertusillo events.

coherently with a mechanism of fracture opening and closure under positive and negative pressure gradients.

6.2 Reservoir-induced seismicity mechanisms

For the Pertusillo lake seismicity, the occurrence of $M_L \leq 2.7$ events, shear-tensile mechanisms and impoundment refill stage seem to suggest a role of pore fluid pressure on the rupture process. However, unlike the fluid injection seismicity, the interpretation of the FMTs obtained for the Pertusillo is complicated because of the large variability of the observed faulting mechanisms (as evidenced by the scattered distribution of the stress axis in the *P*–*T* polar plots). We observe markedly negative NDC percentages during high water levels and general lack of such events (with positive NDC) at low water levels. The prevalence of normal-faulting mechanisms is coherent with the local extensional regime, but the highly variable directions of the *T*-axes (Fig. 2d) contrasts with the orientation of the maximum horizontal stress SH_{max} inferred by breakouts of several wells and of the local normal faults, which coherently strike NW-SE.

Such differences with respect to the CM2 seismicity might be due to the different characteristics and physical mechanism of the Pertusillo. For instance, unlike the CM2 events, the four clusters of Pertusillo affected a relatively large crustal volume, in the order of 50 km^3, that extends from 2.0 to 5.5 km depth. According to the geomechanical modelling of Rinaldi *et al.* (2020), the occurrence of the Pertusillo RIS can be instead explained by poro-elastic volumetric deformations and pore-pressure changes in the buried Apulian carbonates caused by the strong seasonal variations of the lake volume. We speculate that under these conditions (i.e. carbonates affected by widespread systems of fractures filled by pressurized fluids), even small Coulomb stress changes in the source region of the RIS are sufficient to induce slip on small faults and fractures having variable orientations.

In addition, the Pertusillo results could be influenced by rock anisotropy in the source region and/or along the travel path of seismic waves (Šílený & Vavryčuk 2002; Vavryčuk 2005). Shear wave splitting analysis of the Val d'Agri seismicity (mostly for Pertusillo area) has revealed stress-induced crustal anisotropy (i.e. Extensive-Dilatancy Anisotropy model; see Pastori *et al.* 2009) with cracks aligned in the Apennines direction (NW–SE). This information could help to explain the very large CLVD component (compared to ISO) obtained for numerous events and the low percentage (12%) of solutions having ISO and CLVD components with opposite sign.

7 CONCLUSION

We analyse the FMTs of seismicity from the complex and seismic hazard-prone region of Val d'Agri basin, Southern Italy. The study area hosts two well-documented cases of induced microseismicity connected to the Costa Molina 2 injection well of the local giant oilfield (the largest in onshore Europe) and to severe seasonal water level changes of the Pertusillo artificial lake. The examination of final results allows concluding that:

(i) Most of the FMT sources for both CM2 and Pertusillo earthquakes show prevailing NDC components interpreted as shear-tensile sources.

(ii) The injection induced microseismicity associated with the CM2 well is due to the rupture of small faults and fractures of a highly permeable fault zone of a pre-existing thrust fault. We hypothesize that the pore pressure changes in the source area could have been strong enough (i.e. in the order of 10 bar, see Hager *et al.* 2021; Vadacca 2020) to activate small faults and fractures with variable strike and dip, including small structures not optimally oriented for failure in the local stress field.

(iii) The RIS related to the Pertusillo lake can be instead explained by poro-elastic volumetric deformations and pore-pressure changes in strongly fractured and brine-satured limestones, which are caused by the strong seasonal variations of the lake level.

Downloaded from https://academic.oup.com/gji/article/234/3/1617/7115318 by INGV user on 25 May 2023

(iv) Use of appropriate statistical tools methods informs us about resolution of different inversion methods and capacity to discriminate them. The application of these methods in this study provides consistent results for both CM2 and Pertusillo cases, giving greater mining to inversion results. Specifically, they help us to judge the significance of NDC component of the FMT model and to identify the different physical processes underlying seismicity of selected areas.

SUPPORTING INFORMATION

Supplementary data are available at *GJI* online.

Figure S1. Examples of vertical component waveforms from our data set both in (a) and (c) time and (b) and (d) correspondent displacement domain. The (a) and (b) very good/selected and the (c) and (d) bad/rejected seismograms for our FMT analysis are shown.

Figure S2. Results of RMS error analysis for CM2 data. We tested different 1-D local velocity models available in literature of the Val d'Agri region and then we selected and used the model providing the best RMS errors. The tested 1-D velocity models: A (Buttinelli *et al.* 2016; Improta *et al.* 2017), B (1-D best-fitting starting model applied in 3-D tomographic inversion of Improta *et al.* 2017) and C (Valoroso *et al.* 2009). We tested them estimating the FMTs and we expressed the associated uncertainties through normalized RMS residuals between theoretical and estimated amplitudes (Vavryčuk 2014). The RMS errors obtained by using the model A (magenta squares), B (grey circles) and C (light-blue circles) are compared with the earthquake associated with the respective event numbers. The 1-D velocity model A is applied in the text.

Figure S3. Results of RMS error analysis for Pertusillo data. We tested different 1-D local velocity models available in literature of the Val d'Agri region and then we selected and used the model providing the best RMS errors. The tested 1-D velocity models: A (Buttinelli *et al.* 2016; Improta *et al.* 2017), B (Improta *et al.* 2017). We tested them estimating the FMTs and we expressed the associated uncertainties through normalized RMS residuals between theoretical and estimated amplitudes (Vavryčuk 2014). The RMS errors obtained by using the model A (magenta squares), B (grey circles) are compared with the earthquake associated with the respective event numbers. The 1-D velocity model A is applied in the text.

Figure S4. The FMT solutions of CM2 data. The numbers indicate the corresponding event numbers.

Figure S5. The main representative FMT solutions of Pertusillo data. The numbers indicate each main class number in which we are classified the beach balls.

Figure S6. The main representative FMT solutions of CM2 data with the Polarity Resampling. The original input phase is used to generate 100 derived and biased input phase data sets; for each resampled input data set, a separate moment tensor inversion is performed and added to the original results of unbiased input data set. We generate and then perform the seismic moment tensor inversion with additional 100-times resampled input data set that are generated assuming the up to 1 per cent of input phases have wrongly picked polarity. The numbers indicate the corresponding main class number in which we are classified the beach balls (the same in Fig. S4).

Figure S7. The same as in Figure S6, but for the Pertusillo. The numbers indicate the corresponding main class number in which we are classified the beach balls (the same in Fig. S5).

Please note: Oxford University Press is not responsible for the content or functionality of any supporting materials supplied by the authors. Any queries (other than missing material) should be directed to the corresponding author for the paper.

SOFTWARE AVAILABILITY

FMC: Álvarez-Gómez, J.A., 2019. FMC—Earthquake focal mechanisms data management, cluster and classification, *SoftwareX*, **9**, 299-307. doi:10.1016/j.softx.2019.03.008, https://github.com/Jose-Alvarez/FMC.

GMT 4.5.18: Wessel, P. &. Smith, W.H.F., 1998. New, improved version of Generic Mapping Tools released, *EOS Trans. AGU*, **79**(47), p. 579. doi:10.1029/98EO00426, https://github.com/GenericMappingTools/gmt/wiki/GMT-4.5.18.

hybridMT: Kwiatek, G., Martínez-Garzón, P. & M. Bohnhoff, 2016. HybridMT: A Matlab/Shell environment package for seismic moment tensor inversion and refinement, *Seismol. Res. Lett.* doi: 10.1785/022 015 0251; https://www.induced.pl/software/hybridmt, EPOS Platform of Thematic Core Service Anthropogenic Hazards: https://tcs.ah-epos.eu/#app:FOCI_APP.

Matlab: MATLAB 2018a, The MathWorks, Inc., Natick, Massachusetts, USA.

ACKNOWLEDGMENTS

PM-G acknowledges funding from the Helmholtz Association in the frame of the Helmholtz Young Investigators Group SAIDAN (VH-NG-1323). We also thank Prof Elisa Tinti (Università La Sapienza, Roma) for the constructive support. The study has been carried out in the frame of EPOS Thematic Core Service 'Anthropogenic Hazards'.We thank editor and reviewers for critically reviewing the manuscript and suggesting improvements.

DATA AVAILABILITY

The data sets used for this study will be soon available on the EPOS Platform of Thematic Core Service Anthropogenic Hazards (Orlecka-Sikora *et al.* 2020):

https://tcs.ah-epos.eu/#episode:VAL_DAGRI_OIL_FIELD,
https://tcs.ah-epos.eu/#episode:VAL_DAGRI_RESERVOIR
(registration is required).

The coordinates of the oilfield wells are available at:
https://unmig.mise.gov.it/index.php/it/dati/ricerca-e-coltivazione-di-idrocarburi/pozzi-produttivi

REFERENCES

Aki, K. & Richards, P.G., 2002. *Quantitative Seismology,* 2nd edn, W.H. Freeman and Company, San Francisco, CA.

Álvarez-Gómez, J.A., 2019. FMC – Earthquake focal mechanisms data management, cluster and classification, *SoftwareX,* **9,** 299–307.

Amemoutou, A., Martínez-Garzón, P., Kwiatek, G., Rubinstein, J.L. & Bohnhoff, M., 2021. Earthquake source mechanisms and stress field variations associated with wastewater-induced seismicity in Southern Kansas, USA, *J. Geophys. Res. (Solid Earth),* **126**(7), e2020JB021625, doi:10.1029/2020JB021625.

Andersen, L.M., 2001. *A Relative Moment Tensor Inversion Technique Applied to Seismicity Induced by Mining,* Univ. of the Witwatersrand, Johannesburg, South Africa.

Bentz, S., Martínez-Garzón, P., Kwiatek, G., Bohnhoff, M. & Renner, J., 2018. Sensitivity of full moment tensors to data preprocessing and inversion parameters: a case study from the salton sea geothermal field. *Bull. seism. Soc. Am.,* **108**(2), 588–603.

Downloaded from https://academic.oup.com/gji/article/234/3/1617/7115318 by INGV user on 25 May 2023

Buttinelli, M., Improta, L., Bagh, S. & Chiarabba, C., 2016. Inversion of inherited thrusts by wastewater injection induced seismicity at the Val d'Agri oilfield (Italy), *Sci. Rep.,* **6**(1), 37165, doi:.

Cesca, S., Rohr, A. & Dahm, T., 2012. Discrimination of induced seismicity by full moment tensor inversion and decomposition*, J. Seismol.,* **17,** 147–163.

Cucci, L., Pondrelli, S., Freopoli, A., Mariucci, M.T. & Moro, M., 2004. Local pattern of stress field and seismogenic sources in Meandro Pergola basin and in Agri valley (Southern Italy), *Geophys. J. Int.,* **156,** 575–583.

Dost, B., Stiphout, A., Kühn, D., Kortekaas, M., Ruigrok, E. & Heimann, S., 2020. Probabilistic moment tensor inversion for hydrocarbon-induced seismicity in the Groningen Gas Field, the Netherlands, Part 2: application. *Bull. seism. Soc. Am.,* **110**(5), 2112–2123.

Dreger, D.S. & Helmberger, D.V., 1993. Determination of source parameters at regional distances with 3-component sparse network data, *J. geophys. Res.,* **98,** 8107–8125.

Ellsworth, W.L., 2013. Injection-induced earthquakes, *Science,* **341**(6142), doi:10.1126/science.1225942.

Ferranti, L., Palano, M., Cannavo`, F., Mazzella, M.E., Oldow, J.S., Guegue, E. & Monaco, C., 2014. Rates of geodetic deformation across active faults in southern Italy. *Tectonophysics,* **621,** 101–122.

Fischer, T. & Guest, A., 2011. Shear and tensile earthquakes caused by fluid injection, *Geophys. Res. Lett.,* **38**(5), L05307, doi:10.1029/2010GL045447.

Frohlich, C., 1994. Earthquakes with non-double-couple mechanisms, *Science,* **264**(5160), 804–809.

Frohlich, C., 2001. Display and quantitative assessment of distributions of earthquake focal mechanisms. *Geophys. J. Int.,* **144**(2), 300–308.

Guilhem, A., Hutchings, L., Dreger, D.S. & Jonson, L.R., 2014. Moment tensor inversions of M ∼ 3 earthquakes in the Geyser geothermal field, California, *J. geophys. Res.(Solid Earth),* **119**(3), 2121–2137.

Hager, B.H. *et al.* 2021. A process-based approach to understanding and managing triggered seismicity. *Nature,* **595,** 684–689.

Hudson, J.A., Pearce, R.G. & Rogers, R.M., 1989. Source time plot for inversion of the moment tensor, *J. geophys. Res.,* **94**(B1), 765–774.

Improta, L., Bagh, S., De Gori, P., Valoroso, L., Pastori, M., Piccinini, D. & Buttinelli, M., 2017. Reservoir structure and wastewater-induced seismicity at the Val d'Agri oilfield (Italy) shown by three-dimensional Vp and Vp/Vs local earthquake tomography, *J. geophys. Res. (Solid Earth),* **122,** doi:10.1002/2017JB014725.

Improta, L., *et al.*, 2010. Detecting young, slow-slipping active faults by geologic and multidisciplinary high-resolution geophysical investigations: a case study from the Apennine seismic belt, Italy. *J. geophys. Res. (Solid Earth),* **115**(B11). doi: 10.1029/2010JB000871.

Improta, L., Valoroso, L., Piccinini, D. & Chiarabba, C., 2015. A detailed analysis of wastewater-induced seismicity in the Val d'Agri oil field, Italy, *Geophys. Res. Lett.,* **42**(8), 2682–2690.

ISIDe Working Group, 2007. Italian Seismological Instrumental and Parametric Database (ISIDe), *Istituto Nazionale di Geofisica e Vulcanologia (INGV),* doi:10.13127/ISIDE.

Julian, B.R., Miller, A.D. & Foulger, G.R., 1998. Non-double-couple earthquakes 1: theory, *Rev. Geophys.,* **36,** 525–549.

Kass, R.E. & Raftery, A.E., 1995. Bayes factors, *J. Am. Stat. Assoc.,* **90,** 773–795.

Kaverina, A.N., Lander, A.V. & Prozorov, A.G., 1996. Global creepex distribution and its relation to earthquake-source geometry and tectonic origin, *Geophys. J. Int.,* **125**(1), 249–265.

Knopoff, L. & Randall, M.J., 1970. The compensated linear-vector dipole. A possible mechanism for deep earthquakes, *J. geophys. Res.,* **75,** 1957–1963.

Kühn, D., Heimann, S., Isken, M.P., Ruigrok & B. Dost, B., 2020. Probabilistic moment tensor inversion for hydrocarbon-induced seismicity in the Groningen Gas Field, The Netherlands, Part 1: testing, *Bull. seism. Soc. Am.,* **110**(5), 2095–2111.

Kwiatek, G., Martínez-Garzón, P. & Bohnhoff, M., 2016. HybridMT: a Matlab/Shell environment package for seismic moment tensor inversion and refinement, *Seismol. Res. Lett.,* doi:10.1785/0220150251.

Martínez-Garzón, P., Kwiatek, G., Bohnoff, M. & Dresen, G., 2017. Volumetric components in the earthquake source related to fluid injection and stress state, *Geophys. Res. Lett.,* **44**(2), 800–809.

Maschio, L., Ferranti, L. & Burrato, P., 2005. Active extension in Val d'Agri area, Southern Apennines, Italy; implications for the geometry of the seismogenic belt, *Geophys. J. Int.,* **162**(2), 591–609.

Miller, A.D., Foulger, G.R. & Julian, B.R., 1998. Non-double-couple earthquakes 2: observations, *Rev. Geophys.,* **36,** 551–568.

Montone, P., Mariucci, M.T. & Pierdominici, S., 2012. The Italian present-day stress map, *Geophys. J. Int.,* **189,**705–716.

Orlecka-Sikora, B. *et al.*, 2020. An open data infrastructure for the study of anthropogenic hazards linked to georesource exploitation. *Sci. Data,* **7,** 89, doi:10.1038/s41597-020-0429-3.

Pastori, M., Piccinini, D., Margheriti, L., Improta, L., Valoroso, L., Chiaraluce, L. & Chiarabba, C., 2009. Stress aligned cracks in the upper crust of the Val d'Agri region as revealed by shear wave splitting, *Geophys. J. Int.,* **179**(1), 601–614.

Rinaldi, A.P., Improta, L., Hainzl, S., Catalli, F., Urpi, L. & Wiemer, S., 2020. Combined approach of poroelastic and earthquake nucleation applied to the reservoir-induced seismic activity in the Val d'Agri area, Italy. *J. Rock Mech. Geotech. Eng.,* **12**(4), 802–810.

Ross, A., Foulger, G.R. & Julian, B.R., 1996. Non-double-couple earthquake mechanisms at The Geysers geothermal area, California, *Geophys. Res. Lett.,* **23**(8), 877–880.

Rovida, A., Locati, M., Camassi, R., Lolli, B. & Gasperini, P., 2020. The Italian earthquake catalogue CPTI15. *Bull. Earth. Eng.,* **18**(7), 2953–2984.

Rovida, A., Locati, M., Camassi, R., Lolli, B., Gasperini, P. & Antonucci, A., 2021. Catalogo Parametrico dei Terremoti Italiani (CPTI15), versione 3.0. *Istituto Nazionale di Geofisica e Vulcanologia (INGV),* doi:10.13127/CPTI/CPTI15.3.

Royden, L., Patacca, E. & Scandone, P., 1987. Segmentations and configuration of subducted lithosphere in Italy: an important control on thrust-belt and foredeep-basin evolution, *Geology,* **15,** 714–717.

Saraò, A., Cocina, O., Privitera, E. & Panza, G.F., 2010. The dynamics of the 2001 Etna eruption as seen by full moment tensor analysis, *Geophys. J. Int.,* **181**(2), 951–965.

Šílený, J. & Vavryčuk, V., 2002. Can unbiased source be retrieved from anisotropic waveforms by using an isotropic model of the medium? *Tectonophysics,* **356,** 125–138.

Stabile, T.A., Giocoli, A., Lapenna, V., Perrone, A., Piscitelli, S. & Telesca, L., 2014a. Evidences of low-magnitude continued reservoir-induced seismicity associated with the Pertusillo artificial lake (southern Italy), *Bull. seism. Soc. Am.,* **104**(4), 1820–1828.

Stabile, T.A., Giocoli, A., Perrone, A., Piscitelli, S. & Lapenna, V., 2014b. Fluid injection induced seismicity reveals a NE dipping fault in the southeastern sector of the High Agri Valley (southern Italy), *Geophys. Res. Lett.,* **41**(16), 5847–5854.

Vadacca, L., 2020. The altotiberina low-angle normal fault can fail in moderate-magnitude earthquakes as a result of stress transfer from stable creeping fault area, *Geosciences,* **10,** 144. doi: 10.3390/geosciences10040144.

Valoroso, L., Improta, L., Chiaraluce, L., Di Stefano, R., Ferranti, L., Govoni, A. & Chiarabba, C., 2009. Active faults and induced seismicity in the Val d'Agri area (Southern Apennines, Italy), *Geophys. J. Int.,* **178**(1), 488–502.

Valoroso, L., Improta, L., De Gori, P. & Chiarabba, C., 2011. , *J. geophys. Res.,* **116**(B7), doi:10.1029/2010JB007661.

Vavryčuk, V., 2001. Inversion for parameters of tensile earthquakes, *J. geophys. Res.,* **106,** 16,339–316,355.

Vavryčuk, V., 2005. Focal mechanisms in anisotropic media, *Geophys. J. Int.,* **161,** 334–346.

Vavryčuk, V., 2014. Moment tensor decompositions revisited, *J. Seismol.,* **19,** 231–252.

Waldhauser, F., 2001. HypoDD: a computer program to compute double-difference earthquake locations, *USGS Open File Rep* 01-113:2001.

Zoback, M.D., 2007. *Reservoir Geomechanics,* Cambridge University Press, pp449.

Downloaded from https://academic.oup.com/gji/article/234/3/1617/7115318 by INGV user on 25 May 2023